






## Impact of structural complexity and disorder on lattice dynamics and thermal conductivity in the o-Al<sub>13</sub>Co<sub>4</sub> phase

P.-F. Lory <sup>1,2</sup>, V. M. Giordano <sup>3</sup>, P. Gille,<sup>4</sup> H. Euchner <sup>5</sup>, M. Mihalkovič <sup>6</sup>, E. Pellegrini,<sup>1</sup> M. Gonzalez,<sup>1</sup> L.-P. Regnault,<sup>7</sup> P. Bastie,<sup>1,8</sup> H. Schober,<sup>1,9</sup> S. Pailhes <sup>3</sup>, M. R. Johnson,<sup>1</sup> Yu. Grin,<sup>10</sup> and M. de Boissieu<sup>2,\*</sup>

<sup>1</sup>*Institut Laue-Langevin 38000 Grenoble, France*

<sup>2</sup>*Université Grenoble Alpes, CNRS, Grenoble INP, SIMAP, 38000 Grenoble, France*

<sup>3</sup>*ILM, UCBL, CNRS, UMR-5586, 69622 Villeurbanne, Lyon, France*

<sup>4</sup>*Ludwig-Maximilians-Universität München, 80333 Munich, Germany*

<sup>5</sup>*Helmholtz Institute Ulm for Electrochemical Energy Storage, 89081 Ulm, Germany*

<sup>6</sup>*Institute of Physics, Slovak Academy of Sciences, 84511 Bratislava, Slovakia*

<sup>7</sup>*Université Grenoble Alpes, CEA, F-38000, Grenoble, France*

<sup>8</sup>*Université Grenoble Alpes, CNRS, LIPhy, F-38000, Grenoble, France*

<sup>9</sup>*Université Grenoble Alpes, F-38000, Grenoble, France*

<sup>10</sup>*Max-Planck-Institut für Chemische Physik fester Stoffe, Dresden, Germany*



(Received 11 June 2019; revised 29 May 2020; accepted 1 June 2020; published 7 July 2020)

Combining inelastic neutron and x-ray scattering with atomic scale simulation, we report on a comprehensive study of the lattice dynamics and its relationship with the low thermal conductivity of the o-Al<sub>13</sub>Co<sub>4</sub> phase, a periodic approximant (about 100 atoms per cell) to a decagonal quasicrystal. The obtained experimental data, phonon lifetimes, and temperature-independent lattice thermal conductivity can only be fully described by molecular dynamics simulations, using oscillating pair potential, when the disorder of 12 Al sites is properly taken into account. Our results pave the way for a detailed understanding of materials where structural complexity and local disorder are at play.

DOI: [10.1103/PhysRevB.102.024303](https://doi.org/10.1103/PhysRevB.102.024303)

### I. INTRODUCTION

Quasicrystals are long-range-ordered materials, yet without three-dimensional translational symmetry. Since their discovery [1], a lot of progress has been made in the understanding of their atomic structure (see [2] for an introduction). Whether the quasicrystalline long-range order brings in new and specific physical properties remains an open question. Their lattice dynamics is particularly interesting in that respect since both atomic scale simulations and experiments are available. It has been shown experimentally that acoustic phonon modes are well defined for wave vectors smaller than 3 nm<sup>-1</sup> whereas only broad and dispersionless excitations are observed for larger wave vectors, the latter being associated with the crossing of the acoustic branch with pseudo-Brillouin-zone boundaries [3–6]. The crossover between the two regimes is rather abrupt, leading to a rapid broadening of the acoustic excitation. The interpretation of these results is still open, and the very notion of a quantum phonon state is questionable in the high-energy regime, where mode mixing occurs. A similar behavior has been observed in different complex intermetallic alloys (CMAs) [7], such as periodic quasicrystal approximants which share the same “building blocks” as the parent quasicrystal [2,6]. It is also

interesting to point out that most CMAs have a “glasslike” thermal conductivity, with values of the order 1–4 Wm<sup>-1</sup> K<sup>-1</sup> at room temperature, and a weak temperature dependence in the 40–300 K range, instead of the usual umklapp peak observed in simple systems [8–10]. This is very similar to what has been observed in skutterudites or Ge/Si clathrates [11], systems that are also considered as CMA.

In order to study the effect of both structural complexity and disorder on the behavior of acoustic phonons and its relationship with the low thermal conductivity, we here present a study of the orthorhombic o-Al<sub>13</sub>Co<sub>4</sub> phase that is a periodic approximant of the decagonal AlNiCo quasicrystal [12], combining inelastic x-ray and neutron scattering on a single crystal, with molecular dynamic simulations using oscillating pair potentials. The simulation is shown to reproduce the observed dispersion relation, the phonon broadening, and the weakly temperature-dependent thermal conductivity, only when the structural disorder of 12 Al sites over the 100 atoms is properly taken into account.

### II. SAMPLE PREPARATION AND CHARACTERIZATION

A large single grain of the o-Al<sub>13</sub>Co<sub>4</sub> phase has been grown by the Czochralski method. The preparation of the o-Al<sub>13</sub>Co<sub>4</sub> compound was done according to our standard procedure to grow complex metallic alloys (CMAs). The single crystal was grown from an Al-rich high-temperature solution, or

\*Corresponding author: Marc.de-boissieu@simap.grenoble-inp.fr

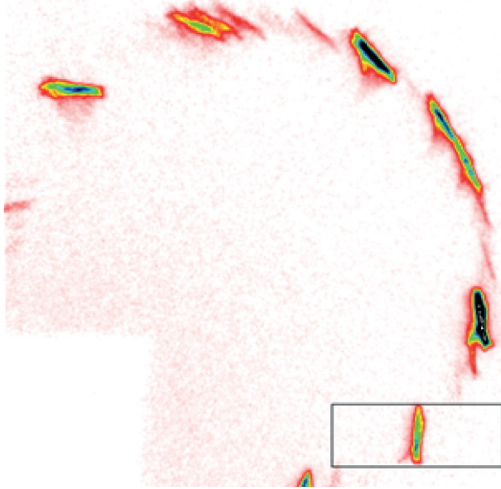


FIG. 1. Hard x-ray Laue diffraction image of the single-crystalline  $o\text{-Al}_{13}\text{Co}_4$  phase. The mosaic spread is measured by the cross section of the Bragg peaks as shown by the gray box.

incongruent melt, of overall composition  $\text{Al}_{85.5}\text{Co}_{14.5}$  that was prepared *ex situ* from bulky pieces of the elements (Al: 4N grade, and Co: 3N-grade, both from CrysTec Berlin, Germany). The synthesis of 26.8 g total mass was done in a 15-mL alumina crucible under Ar 5.0 atmosphere using a rf heating device. After heating to approximately 1200 °C within 1 h, the melt was quenched by switching off the heater. For crystal growth, the synthesized ingot was transferred into a 10-mL alumina crucible and assembled in the fully metal-sealed, Czochralski apparatus. After one week of baking and evacuating a final pressure lower than  $10^{-6}$  mbar was obtained, but crystal growth was done under ambient pressure of Ar 5.0. A [001]-oriented  $o\text{-Al}_{13}\text{Co}_4$  single crystal from a former experiment was used as a seed. Crystal growth was initiated by pulling the wetted seed with a rate of 0.1 mm/h, while rotating the seed and the crucible in opposite directions, with a difference rate of 60 rpm. At the end of the growth run, the crystal was detached from the melt by fast pulling and the crystal was cooled down to room temperature at a rate of 500 K/h. Additional details about the growth process can be found in Gille *et al.* [13].

For this study, we obtained a large crystal with a volume of  $1.5\text{ cm}^3$  (see Fig. 1, Supplemental Material [14]), the quality of which was checked with a hard x-ray diffractometer at ILL in order to determine its bulk mosaicity [15,16]. The use of high energies allows for measuring centimeter-sized samples in transmission geometry. This method allows disorientation of the atomic planes to be detected with a resolution better than  $0.01^\circ$ . Figure 1 shows the diffraction image as measured in the [100]–[010] plane of our sample. A cut is taken along a given direction, and the profile is fitted with a Gaussian function whose width gives the sample mosaic. For the large neutron sample, the mosaic spread was found to be equal to  $0.03^\circ$ , independently of the direction probed.

Physical properties, measured in the range 2–300 K, display a significant anisotropy in electronic transport properties, whereas the lattice thermal conductivity is rather isotropic

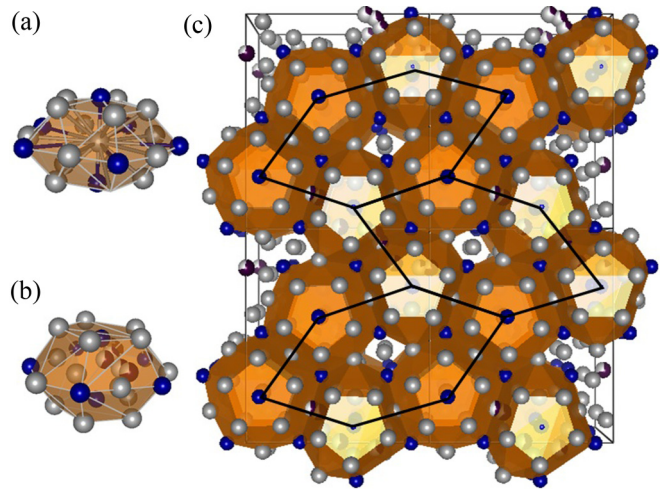


FIG. 2. Crystal structure of  $o\text{-Al}_{13}\text{Co}_4$ . The bipyramidal and linking clusters are shown in (a) and (b), respectively. In (c), the structure is shown in projection on the pseudoquasiperiodic plane. The bipyramidal pentagonal cluster is shown in orange. Gray and blue spheres stand for Al and Co atoms, respectively. Partially occupied Al positions are indicated by black-gray spheres. The large hexagonal tiling, decorated by the cluster, is also indicated.

[9,10]. Similar to other CMA's the lattice thermal conductivity of the sample lies in the range  $2\text{ Wm}^{-1}\text{ K}^{-1}$  and depends only weakly on temperature (see Fig. 13).

### III. ATOMIC STRUCTURE OF THE $o\text{-Al}_{13}\text{Co}_4$ PHASE

Decagonal quasicrystals are characterized by a periodic stacking of two-dimensional (2D) quasiperiodic planes, with periodicities equal to 0.8 nm in the case of the d-AlNiCo quasicrystal [12]. The orthorhombic crystal structure of the  $o\text{-Al}_{13}\text{Co}_4$  phase is a periodic approximant to the decagonal quasicrystal with space group  $Pmn2_1$  and lattice parameters  $a, b, c$  equal to 0.8158, 1.2342, and 1.4452 nm, respectively. In the original refinement by x-ray diffraction [17], the unit cell contains 24 Co and 78 Al atoms resulting in a total of 102 atoms. The  $(b,c)$  plane is the pseudoquasiperiodic plane with two different layers periodically stacked along the  $a$  axis. The structure is also described as a stacking of bipyramidal pentagonal clusters made up of 5 Co and 15 Al atoms, capped by 2 additional Co atoms as illustrated in Fig. 2 [18]. Alternatively, it can be described as a packing of larger pentagonal clusters whose central axis is filled with covalently bonded Co-Al-Co chains as revealed by quantum chemical analysis of the atomic interactions [19] (see Fig. 2 in the Supplemental Material [14]).

The structure has been re-refined recently using x-ray diffraction on a single crystal, and leads to disordered sites as illustrated in the list of coordinates obtained after refinement [20] (see Fig. 3, Supplemental Material [14]). The disorder is observed experimentally as split sites and partial occupancies: there are 24 Co and 64 Al atoms fully occupied and a total of 12.3 Al atoms distributed on 32 sites with partial occupancies as shown in Figs. 2 and 4(a); in this latter one, partially occupied Al sites are indicated by partially filled red spheres. The partially occupied Al

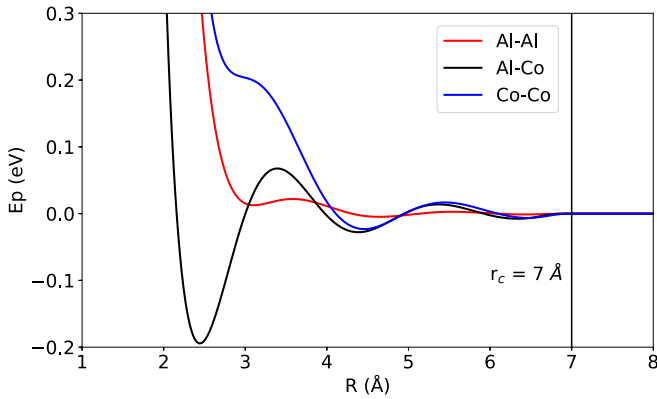


FIG. 3. Semiempirical pair potential for  $o\text{-Al}_{13}\text{Co}_4$ . The Al-Al, Al-Co, and Co-Co pair potentials are shown in red, black, and blue, respectively. The vertical line indicates the cutoff conditions  $r_c = 7 \text{ \AA}$ , such that the potentials and their derivatives are equal to zero.

sites form a chain of atoms running between two Co pentagons. Some of those sites have very low occupancies as seen in the list of coordinates in the Supplemental Material [14]. With this refinement there are 100.3 atoms per unit cell.

#### IV. ATOMIC SCALE SIMULATIONS

All experimental results have been compared with atomic scale simulations using oscillating pair potentials derived from force and energy matching to *ab initio* calculations [18]. The general approach underlying the force-matching method [21,22] is the determination of the material characteristics via *ab initio* calculations. The potentials are fitted specifically to a large number of structures around the  $\text{Al}_{13}\text{Co}_4$  composition and include melted states, as well as high- and low-temperature solids. First, quantities like forces, energies, or stresses are calculated for a reference atomic configuration using *ab initio* methods. Then, a potential model is selected and its parameters are adjusted to reproduce the *ab initio* reference data. The generation of the potential requires an optimization procedure, where the summed squares of the deviations with respect to the reference data are minimized.

Similarly to other intermetallic compounds, we used oscillating pair potentials, which have proved to be very efficient [6,18]. The potentials have the following form:

$$V(r) = \frac{C_1}{r^{\eta_1}} + \frac{C_2}{r^{\eta_2}} \times \cos(kr + \phi). \quad (1)$$

In this equation, there are six parameters, including  $k$ , that were independently determined for all pairs of interactions using the force-matching method. The oscillating part of the potentials correspond to Friedel oscillations [18,23].

The oscillating, semiempirical pair potentials describing the Al-TM (TM = transition metal) interactions in the  $o\text{-Al}_{13}\text{Co}_4$  approximant are shown in Fig. 3. They were used for lattice dynamics calculations and molecular dynamics simulations with a cut-off radius  $r_c$  equal to  $7 \text{ \AA}$ , corresponding to half the size of the smallest simulation cell. At  $r_c$ , the potential and its derivative are forced to zero for every pair

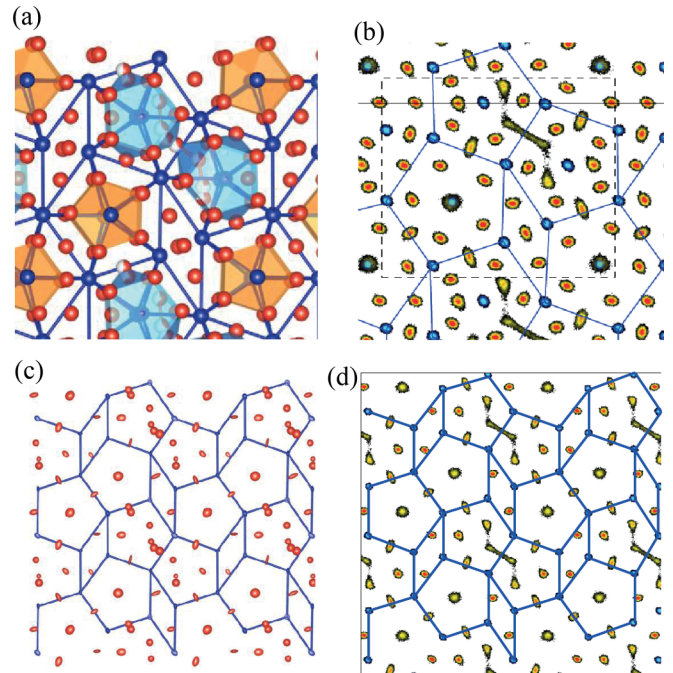


FIG. 4. Atomic structure of the  $\text{Al}_{13}\text{Co}_4$  phase: comparison between the atomic structure derived from x-ray diffraction and molecular dynamics simulation. (a) View of the structure as derived from x-ray diffraction, down the  $a$  pseudofivefold axis. The two different bipyramid clusters are shown in orange and light blue. Al and Co atoms are in red and blue, respectively. Only one cluster type is shown along the  $a$  axis. The two types of cluster are stacked upon each other. The red and white spheres indicate partially occupied Al sites. (b) Projection of the time-averaged density along the  $a$  axis as derived from the molecular dynamic simulation. Highest density is in blue. The low density between two clusters reproduces well the partial sites occupancy (white and red circles) shown in (a) and located between the blue cluster. (c) Atomic structure viewed along the  $(b, c)$  plane for  $a = 0$  as determined by x-ray diffraction data (XRD). Thermal ellipsoids are shown. Notice the large Al thermal ellipsoid in one of the pentagon centers. (d) same as (c) for the averaged electron density extracted from the molecular dynamics simulation.

of interactions by applying an exponential decay function, as shown in Fig. 3.

Two models have been used for comparison with experimental results: the “ordered” one with all sites fully occupied and 102 atoms per cell and the one with partially occupied sites referred to as “disordered” model. The disordered model was generated from a  $3 \times 2 \times 2$  supercell, with the three lattice parameters having similar values ( $a = 24.474 \text{ \AA}$ ,  $b = 24.684 \text{ \AA}$ , and  $c = 28.904 \text{ \AA}$ ). Starting from a  $3 \times 2 \times 2$  supercell of the second model, the disorder was introduced by vacating randomly 19 Al positions on the Wyckoff sites with fractional occupancy. The resulting total number of atoms in the supercell is thus chosen to be 1205, i.e., 100.4 atoms per original unit cell, which is very similar to the experimental findings equal to 100.3. The configuration space is explored using a procedure combining Monte Carlo and molecular dynamics simulations. The Monte Carlo simulations, carried out on a fixed list of sites, including all partially occupied

sites, was carried out with the model including 19 vacancies in the supercell. The Monte Carlo procedure allows all possible configurations to be explored rapidly by swapping atomic sites (vacant site versus occupied site). This is followed by a long molecular dynamics simulation, carried out at 1200 K. We have checked using density functional theory (DFT) calculation that the obtained disordered model indeed has a lower energy than the fully occupied one. This is due to a better matching of the Fermi surface with the pseudogap present in the electronic density of states arising from the presence of vacancies.

The annealing led to an equilibrated structure with no memory of the initial occupancy. This model contains 917 Al and 288 Co atoms and 1.6 vacancies per unit cell, satisfying the experimentally derived density. Its time- and space-averaged spatial occupancy generated by MD simulation matches well the structure derived from x-ray diffraction. We have compared the supercell disordered model with the second atomic structure obtained after refinement against x-ray diffraction data. Averaging and folding back the molecular dynamic simulation carried out at 1200 K to a single unit cell leads to positions and partial occupancies of the Al sites which are in good agreement with those derived experimentally (see Fig. 4). In particular the low atomic density between two clusters shown in Fig. 4(b) reproduces well the partial site occupancies (white and red circles) shown in Fig. 4(a) and located between the blue cluster. The anisotropic ellipsoid displayed by some atoms located on pentagons, shown in Fig. 4(c), are also well reproduced by the simulations as shown in Fig. 4(d).

## V. LATTICE DYNAMICS OF THE $\alpha$ - $\text{Al}_{13}\text{Co}_4$ PHASE

### A. Phonon measurements: Experimental details

A centimeter-sized single crystal of the orthorhombic  $\alpha$ - $\text{Al}_{13}\text{Co}_4$  phase has been used for inelastic neutron scattering experiment on the IN22 triple axis instrument (TAS) at the ILL [24]. We used a graphite (PG002) vertically focusing monochromator and a vertically and horizontally focusing analyzer, with a fixed final neutron momentum  $k_f$  equal to  $2.662 \text{ \AA}^{-1}$ . The setup used on IN22 gave an elastic instrumental resolution of Gaussian shape with a half-width at half-maximum (HWHM) of 0.6 meV, as determined by a measurement of a standard vanadium sample. As shown in Fig. 5, measurements were conducted around the strong Bragg peak 400, scanning in the scattering plane defined by the two directions [H00] and [00L]. The response function  $S(\mathbf{Q}, E)$  was measured along several directions and its temperature dependence was determined in the range 10–550 K.

INS measurements on a conventional neutron TAS scan the  $(\mathbf{Q}, \omega)$  space step by step with a given resolution function. The neutron intensity at a given point  $(\mathbf{Q}_0, \omega_0)$  is given by the convolution product of the instrumental resolution function  $R(\mathbf{Q}, \omega)$  and the neutron scattering function  $S(\mathbf{Q}, \omega)$ , which contains all the information about the dynamics of the system [Eq. (2)]:

$$I(\mathbf{Q}, \omega) = S(\mathbf{Q}, \omega) \otimes R(\mathbf{Q} - \mathbf{Q}_0, \omega - \omega_0). \quad (2)$$

The resolution of a neutron TAS is a four-dimensional function coupling energy and reciprocal space. In order to

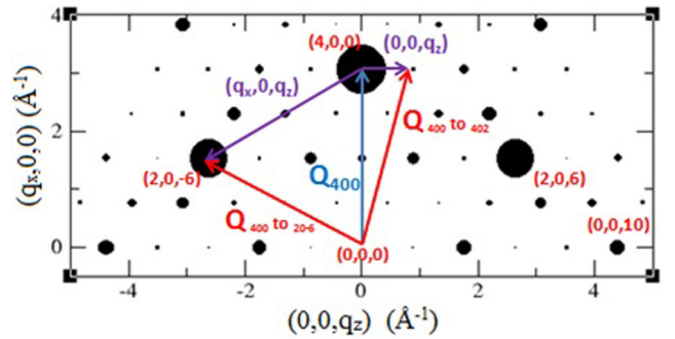


FIG. 5. Diffraction pattern in the (010) plane. Bragg peaks intensities have been calculated for a neutron wave vector equal to  $k_f = 2.662 \text{ \AA}^{-1}$ . Points area are proportional to the nuclear elastic structure factor. The purple arrows around the Bragg peak (400) indicate the two high- and low-symmetry directions along which measurements were carried out.

extract properly the intrinsic position, linewidth ( $\Gamma$  HWHM), and dynamic structure factor (DSF or normalized integrated phonon intensity) from the measured intensity profile, it is necessary to take into account the instrumental resolution function. For dispersing excitations, the resulting instrumental phonon width depends on the relative orientation of the so-called TAS resolution ellipsoid with the slope of the dispersing phonon mode. We have used the RESTRAX software [25] which computes the resolution for a dispersing phonon mode using the instrumental TAS characteristics, the dispersion law of the phonon mode, and Monte Carlo based neutron ray tracing. The resolution function is then convoluted with the dispersion model and phonon modes with finite lifetime. This is achieved by assuming a damped harmonic oscillator model (DHO), which for small broadening can be approximated by a Lorentzian function. The measured linewidth  $\Gamma$  is related to the phonon lifetime by the relation  $\tau = 2\hbar/\Gamma$ .

In this way, we could extract the parameters of the measured excitations using a DHO as response function. The dependency of the phonon instrumental resolution  $\Gamma$ , for an energy transfer equal to 8 meV, as a function of the phonon mode dispersion slope is shown in Fig. 6 and varies between

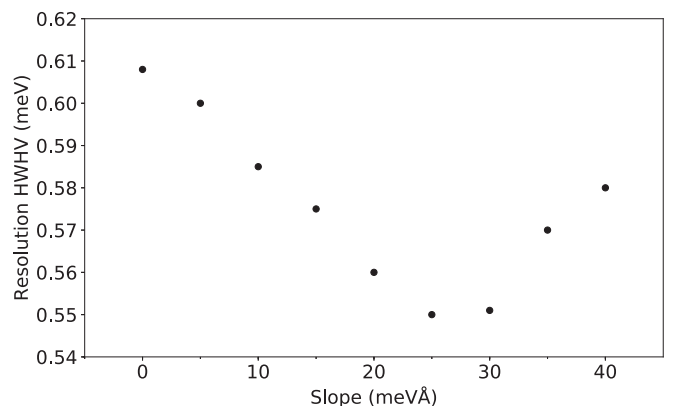


FIG. 6. Evolution of the instrumental resolution  $\Gamma$  (HWHM) for dispersing excitations with different slopes and an energy transfer equal to 8 meV.

0.55 and 0.6 meV (HWHM). The smallest phonon width that can thus be resolved is of the order  $\frac{1}{4}$  times the resolution, i.e., 0.15 meV (HWHM).

The response function  $S(\mathbf{Q}, \omega)$  associated with the emission (absorption) of one phonon in the state  $(s, \mathbf{q})$  is given in Appendix A. The measured response function  $S(\mathbf{Q}, \omega)$  is then the summation over all phonon modes. For an acoustic long-wavelength excitation measured nearby a Bragg peak at a position  $\mathbf{Q} = \mathbf{Q}_{\text{Bragg}} + \mathbf{q}$  it can be shown that the response function integral over the measured phonon peaks reads as

$$\int S_{q,s}(\mathbf{Q}, \omega, T) d\omega \approx (\mathbf{Q} \cdot \sigma_{\mathbf{q},s})^2 |F_{\text{Bragg}}|^2 \frac{n(\omega_{s,\mathbf{q}})}{\omega_{s,\mathbf{q}}}, \quad (3)$$

where  $\sigma_{\mathbf{q},s}$  is the phonon mode polarization,  $F_{\text{Bragg}}$  the Bragg peak structure factor,  $n(\omega_{s,\mathbf{q}})$  the phonon Bose occupation factor, and  $\omega_{s,\mathbf{q}}$  the phonon mode energy. We can define a normalized dynamical structure factor (DSF) as

$$\text{DSF}_{q,s}(\mathbf{Q}, \omega, T) = \frac{\omega_{s,\mathbf{q}}}{Q^2 n(\omega_{s,\mathbf{q}})} \int S_{q,s}(\mathbf{Q}, \omega, T) d\omega. \quad (4)$$

This is an important expression allowing to identify unambiguously the acoustic character of a mode. In the long-wavelength limit this normalized DSF remains constant. This normalized intensity proved to be essential in evidencing the abrupt crossover between the acoustic and opticlike regime of phonons in quasicrystals [3–6].

Inelastic x-ray scattering studies were performed at the ID28 beam line of the European Synchrotron Radiation Facility (ESRF) in Grenoble [26] using a single-crystal specimen of size  $300 \times 300 \times 300 \mu\text{m}^3$  that was extracted from the large single crystal. The sample was aligned such as to allow measurement of the longitudinal excitations in both the pseudoquasiperiodic and pseudoperiodic directions. An energy resolution equal to 1.8 meV (FWHM) was achieved with the Si(12,12,12) reflection monochromator and analyzer. Energy transfers in the range  $-20$  to  $40$  meV were measured at fixed momentum transfer by varying the incident energy while keeping the final energy fixed. Using nine spherical analyzer crystals, multiple values of  $\mathbf{Q}$  were simultaneously measured. However, only data from three analyzers were considered in the analysis of LA phonons. A set of slits ( $60 \times 30 \text{ mm}^2$ ) define the  $Q$  resolution for each analyzer, giving  $dQ = 0.05 \text{ \AA}^{-1}$ . Contrary to TAS instruments, here the resolutions in energy and momentum are decoupled [27,28], facilitating the measurement of the longitudinal acoustic modes where a good resolution in  $\mathbf{Q}$  is required. We have used the same fitting procedure presented in the Supplemental Material of Pailhes *et al.* [29]. We numerically convolute a phonon cross-section model with the instrumental resolution which now can be separated in two independent energy and  $Q$  contributions. The elastic energy resolution of the instrument was determined using a plexiglas sample. For the  $Q$  resolution, we used an envelope which is a Gaussian function whose characteristics depend on the phonon dispersion and the size of the slits placed in front of the analyzers. All data and fitted curves are presented in the Supplemental Material, Sec. S-III [14].

## B. Phonon simulations

Within the harmonic approximation we used the oscillating pair potentials to calculate the phonon frequencies and eigenvectors by diagonalization of the dynamical matrix [30]. They can then be used to calculate the scattering function  $S(\mathbf{Q}, \omega)$  by applying the appropriate experimental scale factors. For the ordered model, a  $2 \times 1 \times 1$  supercell [volume ( $16.33 \times 12.342 \times 14.452$ )  $\text{\AA}^3$ ] containing 204 atoms has been used, while for the disordered model, a  $3 \times 2 \times 2$  supercell was used with a volume equal to ( $24.474 \times 24.684 \times 28.904$ )  $\text{\AA}^3$  and containing 1205 atoms. The simulated  $S(\mathbf{Q}, \omega)$  function is then convoluted by the experimental resolution function, a Gaussian in the case of inelastic neutron scattering and a Lorentzian in the case of inelastic x-ray scattering.

In a second approach we simulated the lattice dynamics using atomic scale molecular dynamics (MD) simulations. We have produced an atomic trajectory using the LAMMPS code [31] and the same, semiempirical, pair potentials as for the above diagonalization. Moreover, we have used the NMOLDYN package [32] to compute the scattering functions  $S(\mathbf{Q}, \omega)$  and  $S(\mathbf{Q}, t)$ . To obtain a good representation of this function, it is necessary to define an adequate sampling in space and time in the trajectory. For example, by building a large enough supercell, we can take into account phonons with long wavelengths, commensurate with the supercell: large supercells allow a fine sampling of the Brillouin zone. The total time of the simulation defines the energy resolution. In MD simulations we simulated a supercell of dimensions ( $196.613 \times 150.239 \times 171.676$ )  $\text{\AA}^3$  during 1 ns with a time step of 2 fs. These conditions allow to compute the  $S(\mathbf{Q}, t)$  and  $S(\mathbf{Q}, \omega)$  spectra with a sampling ( $\Delta Q = 0.01 \text{ \AA}^{-1}$  and  $\Delta E = 0.02$  meV) suitable for comparison with experimental measurements. The main advantage of the MD simulation is that it takes into account all harmonic and anharmonic processes. Thus, finite phonon lifetime and the resulting broadened  $S(\mathbf{Q}, \omega)$  response function can be simulated. The MD simulation can also be used with NMOLDYN to directly compute the intermediate  $S(\mathbf{Q}, t)$  function, from which phonon frequencies and lifetimes can be extracted. We stress that MD simulations do take into account all anharmonic processes involving two, three, four, and more phonon processes. The main well-known drawback of the MD simulations is that phonon eigenvectors are not accessible.

## C. Experimental results

Figure 7 summarizes the inelastic scattering results with the extracted dispersion relation [Figs. 7(a), 7(d), and 7(g)] together with selected constant  $Q$  energy scans in transverse and longitudinal configurations. Experimental data are compared with harmonic simulation of the scattering function using the disordered model. The simulation results are convoluted by the instrumental resolution (Gaussian for neutron and Lorentzian for x rays) and a single scale factor is applied for all scans. Both the dispersion relation and the inelastic scattering intensity distribution (a much more difficult test) are well reproduced as shown in Fig. 7 and in Appendix C, Fig. 17.

This is the case for transverse acoustic (TA) modes propagating along the [001] direction and polarized along the

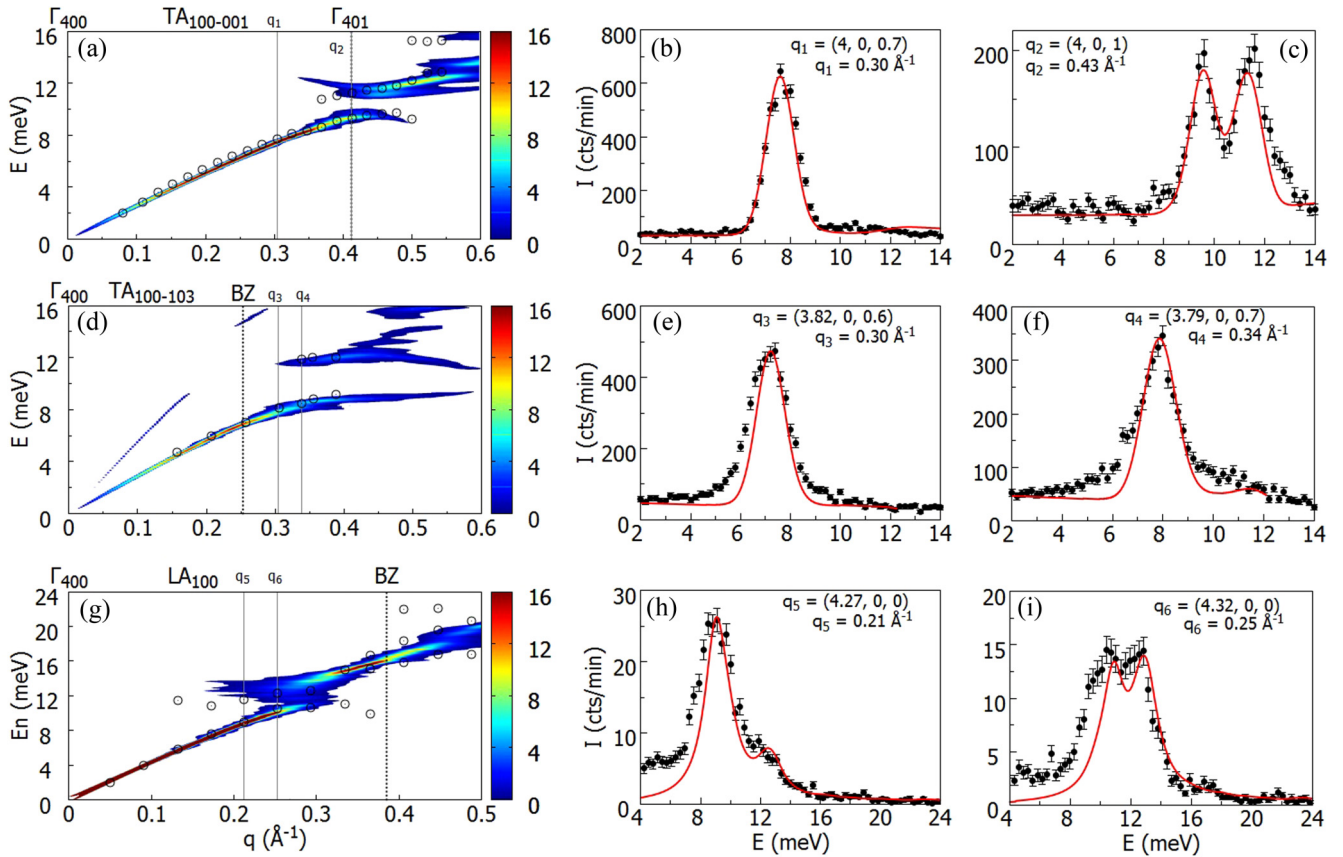


FIG. 7. Dispersion relation and inelastic scattering function for  $o\text{-Al}_{13}\text{Co}_4$ : comparison between experiment and harmonic simulations using the disordered model for TA modes propagating along the [001] (a)–(c) and [103] (d)–(f) directions. LA modes propagating along [100] are displayed in (g)–(i). The measured dispersion relation (black dots) is compared to the harmonic simulation using the disordered model shown as a color-coded curve [(a), (d), (g)]. The measured scattering function  $S(\mathbf{Q}, \omega)$  (black dots) is compared to the simulated one after convolution by the instrumental resolution (red line) [(b), (c), (e), (f), (h), (i)]. The same scale factor has been applied for all simulations. The agreement between simulation and experiment is very good, except for panel (f), where the observed Lorentzian shape is not reproduced by the simulation. Experimental results of (a)–(f) have been obtained by inelastic neutron scattering and those of (g)–(i) by inelastic x-ray scattering.

[100] direction, where a clear gap opening is observed at the zone center (401) seen in Figs. 7(a)–7(c). The acoustic excitation is resolution limited up to  $0.4 \text{ \AA}^{-1}$ , while there is an intensity transfer from the acoustic to the optic branch, typical of an anticrossing of two phonon branches with different symmetry, very well reproduced by the simulation. A more detailed summary of the results, in terms of evolution of the DSF and phonon width, is presented in Fig. 8. For phonons propagating along the high-symmetry directions, we observe a clear intensity transfer between the acoustic and optic modes, resulting from an anticrossing [Fig. 8(a)] (see also a larger set of neutron data in Appendix C, Fig. 17). The extracted width ( $\Gamma$  HWHM) is very small, much below the instrumental resolution, which is of the order  $0.55 \text{ meV}$  (HWHM) at best. Taking as a smallest measurable width  $0.15 \text{ meV}$  (HWHM), we can conclude that the phonon width is resolution limited for wave vectors smaller than  $0.4 \text{ \AA}^{-1}$ .

The same is true for LA modes propagating along the [100] direction where also a well-defined gap is observed, Figs. 7(g)–7(i). The agreement is also excellent at higher energy where the disorder introduced in the model reproduces well the observed, broad, optic excitations (the ordered model would predict too narrow ex-

citations, see Appendix B for a full discussion on this point).

A quite different behavior is observed for TA modes propagating along the [103] direction which, contrary to the two other directions, has a low symmetry [Figs. 7(d)–7(f)]. The interaction and anticrossing with an optical excitation is less clear as illustrated in Figs. 8(c) and 8(d) (see also Appendix C, Fig. 17). Whereas the normalized DSF is constant, an abrupt broadening of the excitations is observed for wave vectors larger than  $0.25 \text{ \AA}^{-1}$ . The constant DSF value indicates that the mode still has an acoustic character, but its lifetime decreases very rapidly in a way very similar to the case of quasicrystals. At  $q = 0.34 \text{ \AA}^{-1}$  [ $\mathbf{Q} = (3.79, 0, 0.7)$ , Fig. 7(f)], the measured acoustic excitation presents a significant broadening with an extracted width equal to  $0.6 \text{ meV}$  (HWHM), much larger than the instrumental sensitivity (see also Fig. 8) and with a Lorentzian shape that is characteristic of a damped harmonic oscillator (DHO).

That the signal for acoustic phonons propagating along the low-symmetry direction going from 400 to 206 shows a DHO profile with a very clear Lorentzian tail is best evidenced when compared with the measurements carried out for a similar  $q$  and energy transfer but for phonons propagating along

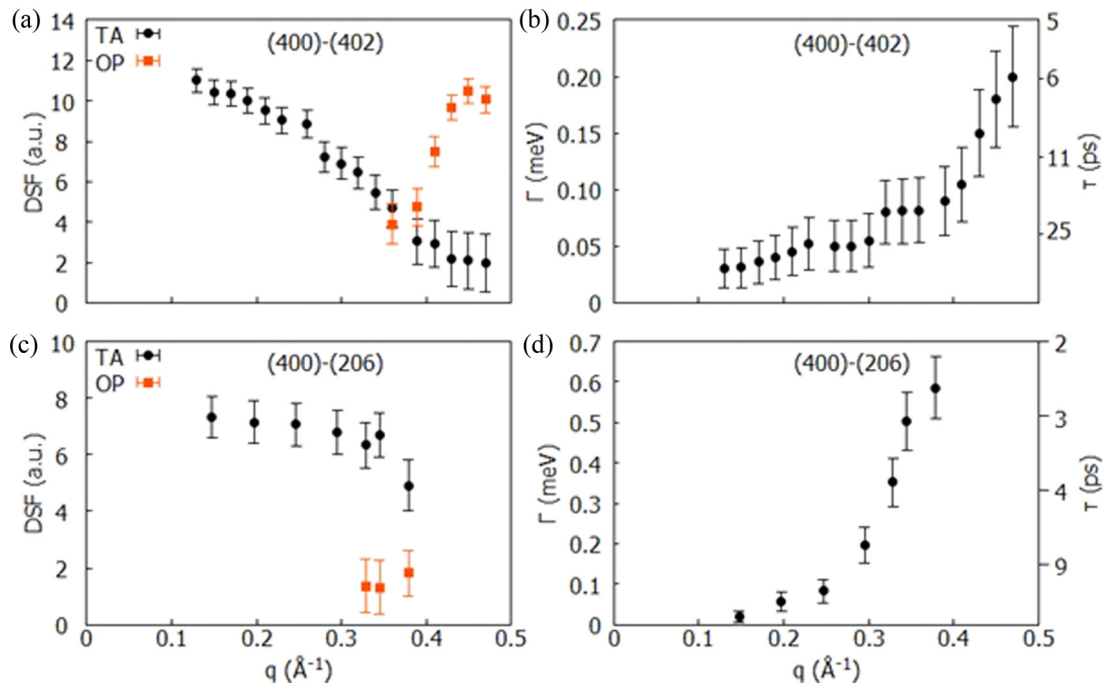


FIG. 8. Evolution of the DSF and width  $\Gamma$  (HWHM) of the inelastic neutron scattering signal. (a), (b) Measurement for phonon modes propagating along the high-symmetry direction [001] along  $\Gamma_{400 \rightarrow 402}$ . There is an intensity transfer from the transverse acoustic (TA) to the optic (OP) mode at the anticrossing region (from 0.35 to 0.45  $\text{\AA}^{-1}$ ). The linewidth of the TA excitations is limited by the instrumental resolution. (c), (d) Measurement for phonon modes propagating along the low-symmetry direction  $\Gamma_{400 \rightarrow 206}$ . There is a clear and rapid broadening of TA excitations.

the high-symmetry direction from 400 to 402, as illustrated Fig. 9(a): in this case the measured signal is limited by the instrumental resolution and presents a Gaussian profile.

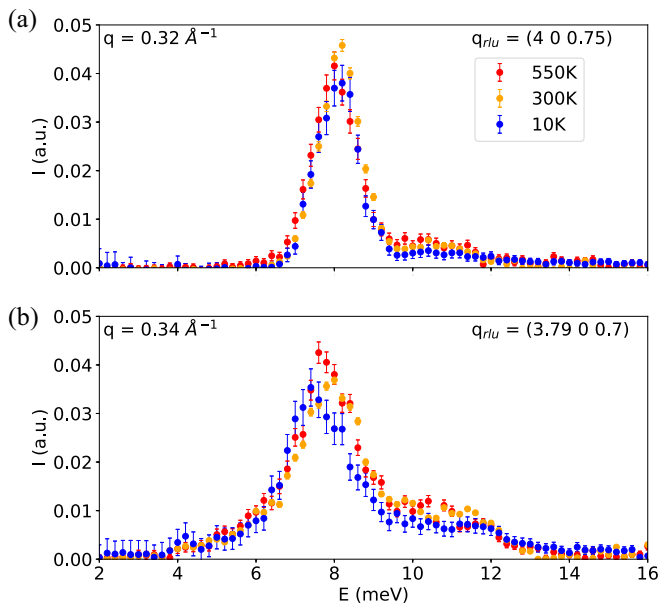


FIG. 9. Comparison of inelastic neutron scattering spectra, corrected for the Bose occupation factor, measured for temperatures in the range 10–550 K. (a) TA phonon measured along the high-symmetry direction [001] from the 400 Bragg peaks; (b) TA phonon measured along the low-symmetry direction [103] from the 400 Bragg peaks.

On the other hand, when measured along the low-symmetry direction [Fig. 9(b)], the signal is significantly broader with a clear Lorentzian tail, characteristic of the DHO profile. At  $q = 3.4 \text{ nm}^{-1}$  [ $\mathbf{Q} = (3.79, 0, 0.7)$ ], the extracted phonon width  $\Gamma$  (HWHM) is equal to 0.6 meV, leading to a phonon lifetime equal to 1.1 ps. At this  $q$  point the phonon wavelength is equal to 1.9 nm and the dispersion relation has already bent over, reducing the phonon group velocity from  $4230 \text{ ms}^{-1}$  in the long-wavelength limit to  $1515 \text{ ms}^{-1}$ . This leads to a phonon mean-free path equal to 1.7 nm, i.e., less than two unit cells and only one phonon wavelength.

The set of raw data used in this section, together with the obtained fit is displayed in Sec. III of the Supplemental Material [14].

In order to determine the phonon scattering mechanism at play, we have carried out a measurement of the temperature dependence of phonon modes and lifetime between 10 and 550 K. Indeed, if it results from anharmonicity, the three-phonon normal ( $N$ ) and umklapp ( $U$ ) scattering processes should display a phonon lifetime that varies as  $1/T$  in the high-temperature limit. On the other hand, phonon scattering on defects just depends on the defect concentration and is temperature independent [33].

As can be seen in Fig. 9, where all scans from 10 to 550 K have been superimposed and renormalized by the Bose occupation factor, the signal does not change with temperature: neither the intensity nor the width does change. In particular, in Fig. 9(b) the low-energy part, which displays a clear Lorentzian tail, does not evolve with temperature: we can thus conclude that the phonon lifetime is temperature independent and thus does not originate from  $N$  or  $U$  processes.

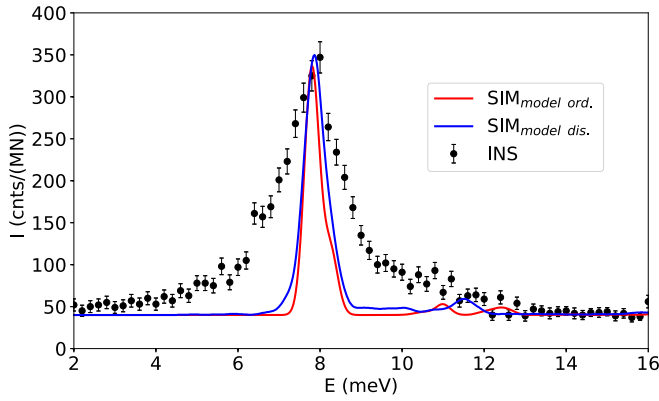


FIG. 10. Constant  $Q$ , energy scan of TA phonon modes propagating along the [103] low-symmetry direction at  $q = 0.34 \text{ \AA}^{-1}$  for  $o\text{-Al}_{13}\text{Co}_4$ . Comparison between the 300-K measurement (black dots) and MD simulations using the ordered (red line) and disordered (blue line) models with a very narrow convolution.

#### D. Comparison with simulations

As already mentioned in the previous section, experimental data have been compared with harmonic simulations using the oscillating pair potentials and the disordered model as displayed in Fig. 7. As can be seen both the dispersion relation and the intensity distribution (a much more sensitive test) are very well reproduced by the simulations. It has to be noticed that a single scale factor has been used for all the simulation. A larger set of data, comparing experiment and simulation for neutron data, is displayed in Appendix C, Figs. 17 and 18.

For modes propagating along high-symmetry directions and for polarization in the transverse [Figs. 7(a)–7(c)] and Fig. 17 left panel, or longitudinal [Figs. 7(h) and 7(i)] direction, the overall agreement is excellent: the acoustic character at long wavelength, the anticrossing, and intensity transfer between the acoustic and optic excitations are perfectly reproduced. Since the measured acoustic modes are resolution limited, their width is also well accounted for once the simulation is convoluted by the experimental resolution.

The situation is quite different for transverse modes propagating along the low-symmetry direction. Whereas the overall dispersion is well reproduced, the harmonic simulations fail to reproduce the mode broadening and Lorentzian tail as illustrated in Figs. 7(e) and 7(f), red lines, and Fig. 17, right panel.

A detailed comparison is presented in Fig. 10, where the harmonic simulation has been convoluted by a narrow Gaussian. Although the simulation with the disordered model is slightly broader than the one with the ordered model, only one major acoustic contribution is contributing in the simulated spectra. A few much weaker opticlike excitations are also visible, but with a negligible intensity. The observed broadened signal thus does not result from the superposition of several optical modes, as was observed at higher energies or for instance in the ZnMgSc icosahedral quasicrystal [6]. These simulations justify the interpretation of the data in terms of a single damped harmonic oscillator. As shown hereafter this Lorentzian broadening can only be reproduced when

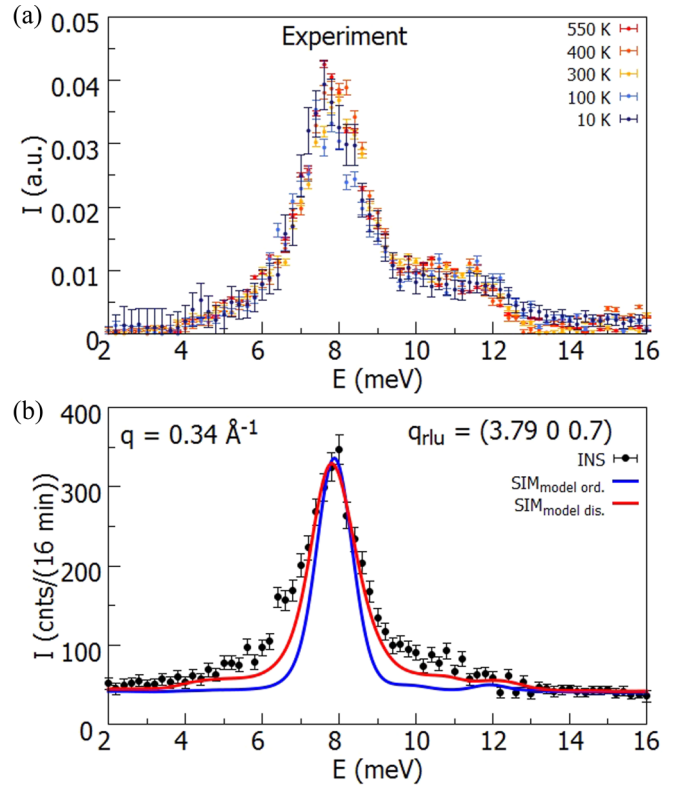


FIG. 11. TA phonons modes propagating along the [103] low-symmetry direction at  $q = 0.34 \text{ \AA}^{-1}$  for  $o\text{-Al}_{13}\text{Co}_4$ . (a) Temperature evolution of the measured signal between 10 and 550 K (a), once renormalized by the Bose occupation factor. (b) Comparison between the 300-K measurement (black dots) and MD simulations using the ordered (blue line) and disordered (red line) models.

performing molecular dynamics on a model that includes the disorder.

To pinpoint the origin of the observed lifetime, and in particular the respective roles of the structural complexity and disorder, we have carried out molecular dynamics simulations using the same oscillating pair potentials. The MD simulation takes into account all phonon scattering processes, from which, using both the ordered and disordered models, the scattering function is extracted and compared to the experimental data in Fig. 11. Whereas the simulation with the ordered model failed to reproduce the measured signal, the disordered model accounts much better for the experimental broadening as shown by the red curve in Fig. 11(b). In particular, the Lorentzian-type tail is now much better reproduced.

This is even more true when the temperature dependence of the signal is simulated. In order to avoid unnecessary Fourier transform termination effects, we compute the intermediate scattering function  $S(\mathbf{Q}, t)$ , which is displayed in Fig. 12 for  $\mathbf{Q} = (3.79, 0, 0.7)$ . The oscillating part of the simulated  $S(\mathbf{Q}, t)$  signal corresponds to the TA mode frequency, whereas the phonon lifetime is extracted by fitting the exponential decay of the signal as shown by the black line in Fig. 12. The temperature dependence of the phonon lifetime is markedly different for the ordered and disordered models. In the ordered model the phonon lifetime is equal to 2.5 and 8.4 ps for temperatures equal to 300 and 100 K, respectively, and



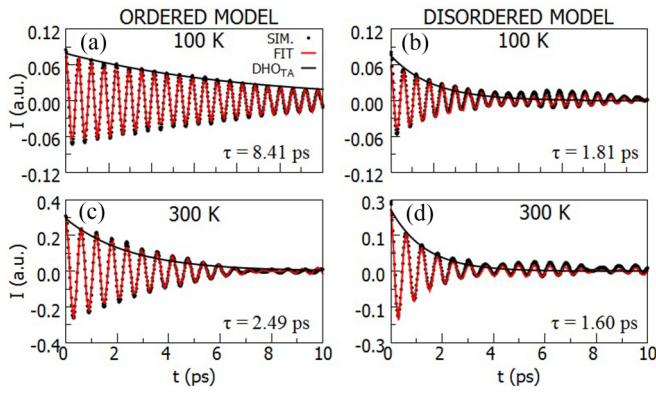


FIG. 12. MD simulated intermediate scattering function  $S(\mathbf{Q}, t)$  in  $\text{o-Al}_{13}\text{Co}_4$  for  $\mathbf{Q} = (3.79, 0, 0.7)$  at 100 and 300 K for the ordered (a), (b) and disordered (c), (d) models. The resulting signal originates from TA phonon mode propagating along the low-symmetry direction  $[103]$  and for  $q = 0.34 \text{ \AA}^{-1}$ .

thus varies as  $1/T$ , as expected for anharmonic three-phonon processes. In the disordered model the phonon lifetimes for the same temperatures are equal to 1.6 and 1.8 ps, respectively, i.e., they are almost temperature independent, as expected for phonon scattering on defects, and in good agreement with the experiment. Introducing the disorder in the modeling thus turns out to be a crucial parameter. We note that a similar influence of disorder on phonon dispersion relations has been observed for the complex  $\text{Zn}_{11}\text{Mg}_2$  phase [34].

In order to get a first atomistic analysis of the differences observed between the high- and low-symmetry directions, we have computed the eigenvectors for modes nearby  $q = 3.7 \text{ nm}^{-1}$  in the simpler ordered model. Whereas along the high-symmetry direction both the acoustic and optical excitations have a characteristic ‘‘antiphase’’ pattern of motion of a stationary wave at the Brillouin zone boundary, involving the entire unit cell (see Supplemental Material movie [14]), modes propagating along the low-symmetry directions involve mainly a large amplitude motion of atoms located inside the clusters (see Supplemental Material movie [14]). There is clearly a symmetry restriction leading to the anticrossing of two branches for high-symmetry directions, whereas mode mixing is more likely for the low-symmetry direction. This, however, requires further analysis to be fully understood.

## VI. LATTICE THERMAL CONDUCTIVITY OF THE $\text{o-Al}_{13}\text{Co}_4$ PHASE

Finally, the lattice thermal conductivity has been simulated using the MD simulations with the oscillating potentials and the Green-Kubo method for both the ordered and disordered models (see Supplemental Material, Sec. II for details [14], see also Refs. [3–11] therein). The computed lattice thermal conductivity at room temperature for  $\text{o-Al}_{13}\text{Co}_4$  is found to be equal to 1.7 and  $1.2 \text{ Wm}^{-1} \text{ K}^{-1}$  for the ordered and disordered models, respectively, in good agreement with the average experimental value of the order  $2 \text{ Wm}^{-1} \text{ K}^{-1}$  [9]. However, whereas the ordered model displays a significant temperature dependence of the lattice thermal conductivity,

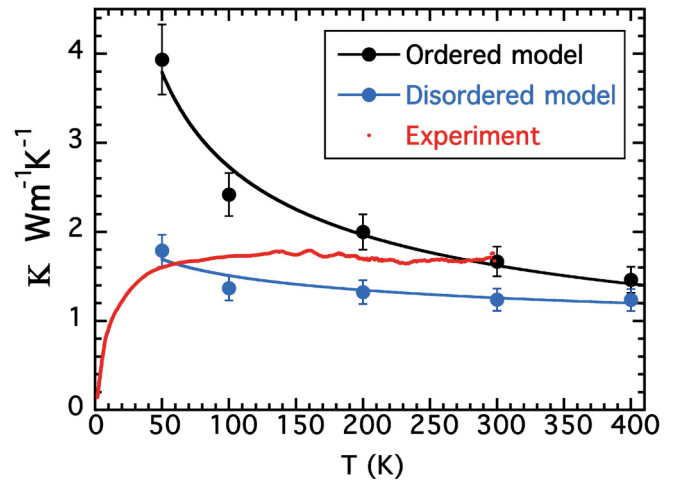


FIG. 13. Comparison between the simulated and experimental temperature dependence of the phonon thermal conductivity in  $\text{o-Al}_{13}\text{Co}_4$  (experimental data from [9]). Simulations have been carried out using the Green-Kubo method with the ordered (black circles) and disordered (blue circles) models. The solid line is a fit with a power law (see text).

varying as  $T^{-0.50}$ , the disordered model displays an almost constant value of the thermal conductivity ( $T^{-0.1}$ ), in good agreement with both the experiment and the computed phonon lifetimes (see Fig. 13).

It is worth pointing out that the  $T^{-0.50}$  dependence simulated with the ordered model departs significantly from a  $1/T$  decay expected if only  $U$  processes were active as shown by simulations. It is similar to the case of mass disorder in simple systems [35] and this suggests that scattering mechanisms, with a weaker temperature dependence, are at play as a result of the structural complexity (see also [36]).

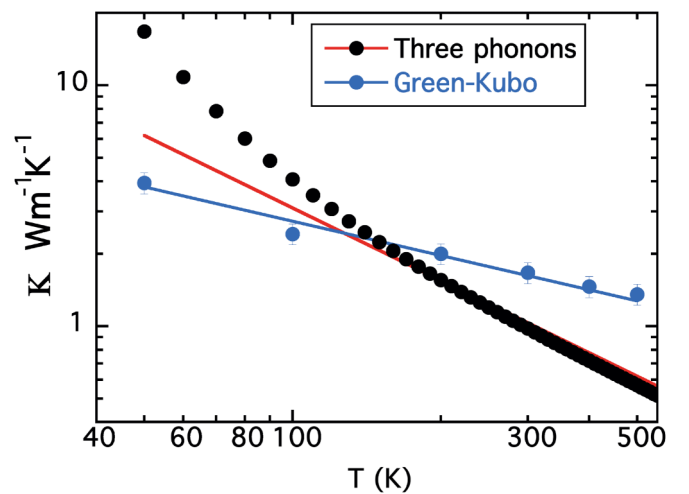


FIG. 14. Total lattice thermal conductivity simulated by the Green-Kubo method in  $\text{o-Al}_{13}\text{Co}_4$  for the ordered model (blue dots). This is compared to the three-phonon contribution as obtained by the ALAMODE simulation on the same model (black dots). The red line represents the  $1/T$  decay, whereas the blue line is a  $T^{-0.50}$  decay.

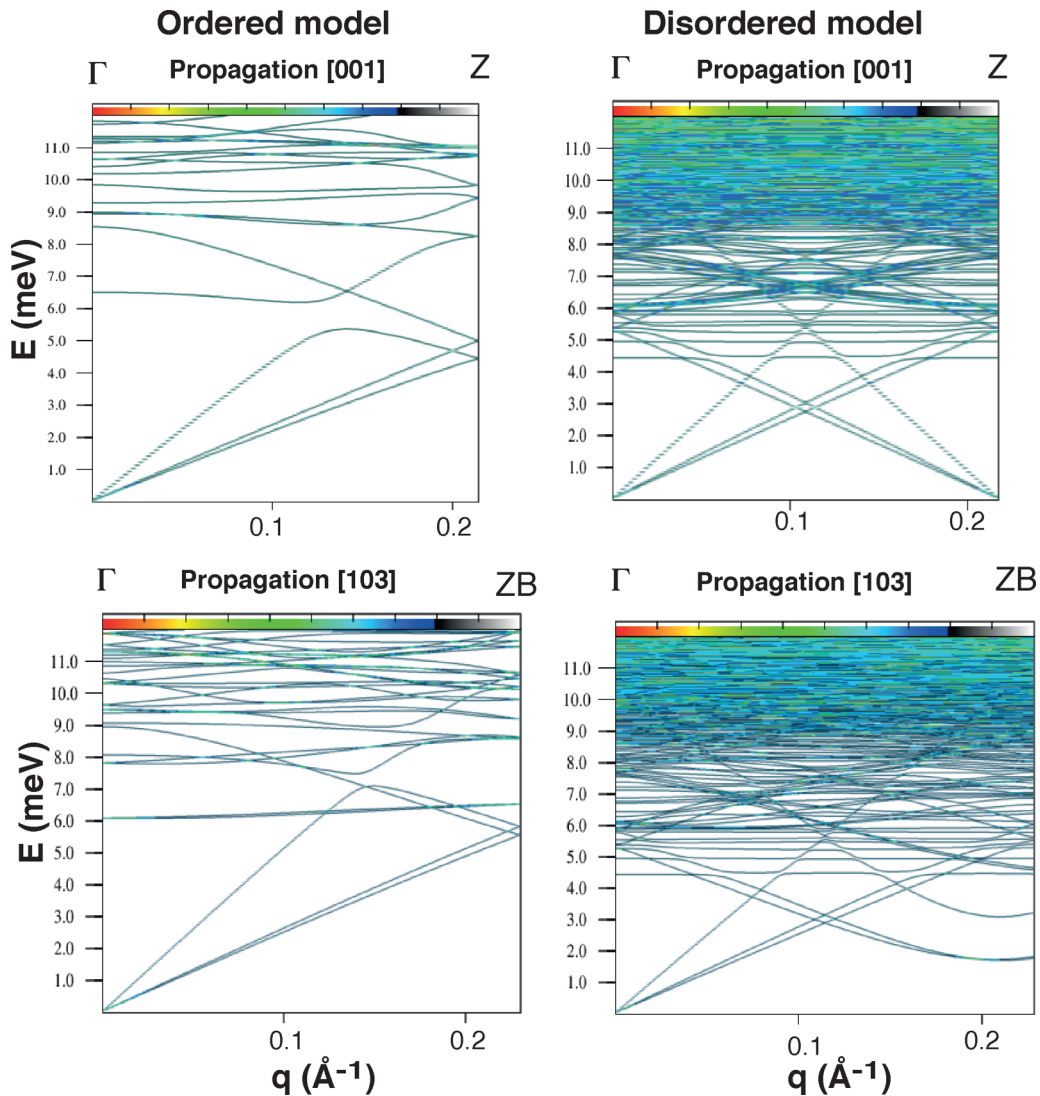


FIG. 15. Comparison of the dispersion relation for the ordered and disordered model (left and right panel, respectively) for modes propagating along the [001] direction (top panel) and the low-symmetry [103] direction for o- $\text{Al}_{13}\text{Co}_4$ .

In order to evaluate the origin of this temperature dependence, we have computed the three-phonon contribution to the lattice thermal conductivity using the *ALAMODE* code introduced by Tadano *et al.* [37]. Within the code, the Boltzmann transport equation (BTE) is solved in the relaxation time approximation, describing the interaction potential by harmonic and third-order force constants. These force constants are obtained by displacing different atoms out of their equilibrium position. In case of the harmonic force constants displacements of  $0.02 \text{ \AA}$  were introduced into the unit cell, while displacements of  $0.04 \text{ \AA}$  were used to determine the third-order force constants.

In fact, third-order force constants were considered up to the next-nearest-neighbor shell (up to  $5.3 \text{ \AA}$ ), meaning a total of 10355 third-order force constants, while 204 harmonic force constants were included, accounting for the full interaction range. Due to this large number of force constants and the corresponding increase in computing time for solving the BTE, only simulations of the ordered model could be carried

out. To enable direct comparison with the above-discussed MD simulations, and due to the fact that determination of such a large amount of force constants by DFT would be extremely costly, we have used the same oscillating pair potential that was used for the MD calculations to determine the interatomic force constants. Finally, the lattice thermal conductivity was determined for a  $5 \times 5 \times 5$   $k$ -point mesh in reciprocal space. The results of the previously discussed Green-Kubo approach and the three-phonon contribution are compared in Fig. 14. There is a clear difference in the temperature dependence of both models. While the three-phonon simulation leads to a decay that is slightly faster than the  $T^{-1}$  expected in simple systems, in the Green-Kubo approach the decay follows a much weaker  $T^{-0.50}$  decay. In principle, in the Green-Kubo approach all contributions to the lattice thermal conductivity are taken into account, this includes in particular higher-order phonon-phonon scattering, but also two-phonon-like scattering that could be brought in by the structural complexity. The exact reasons for these differences, however, still remain to be elucidated.

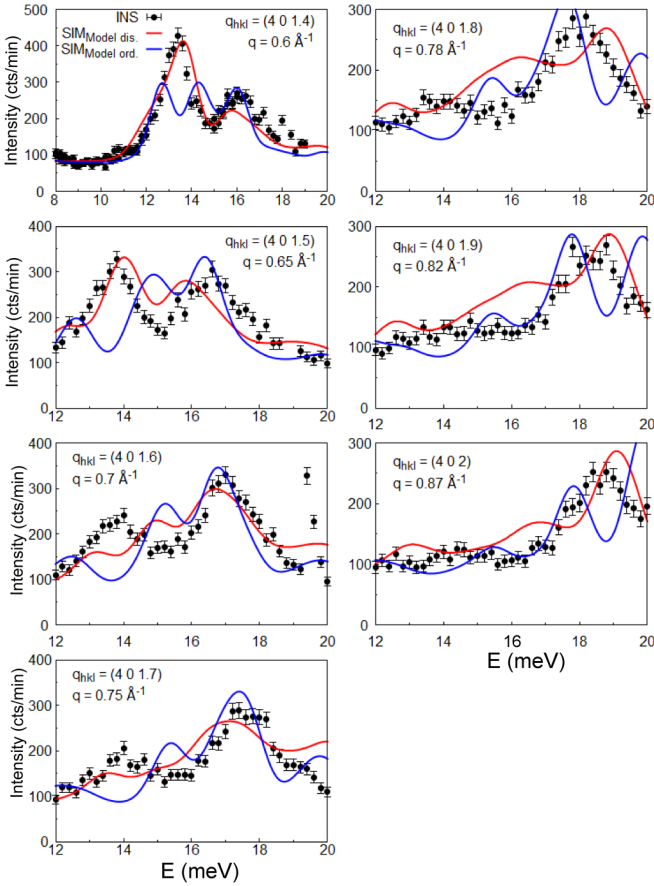


FIG. 16. Comparison between constant  $Q$  inelastic neutron scattering measurements and harmonic simulations using oscillating pair potentials for both the ordered (blue line) and the disordered (red line) models for  $\alpha$ - $\text{Al}_{13}\text{Co}_4$ . Measurements are for modes propagating along the high-symmetry direction [001].

A preliminary study of the  $T$  and  $q$  dependencies of the phonon mode broadening already shows that they differ from the expected form used for simple systems. Introducing the disorder decreases dramatically the temperature dependence of the thermal conductivity. Understanding these results requires, however, a full analysis of the energy and temperature dependence of the phonon lifetimes in both models.

## VII. CONCLUSION

In conclusion, combining inelastic neutron and x-ray scattering, we presented the lattice dynamics of the  $\alpha$ - $\text{Al}_{13}\text{Co}_4$  phase, a structurally complex intermetallic compound, approximant to the decagonal quasicrystalline phase. Within the harmonic approximation and using oscillating pair potential, the phonon dispersion relation and the intensity distribution of the response function are well reproduced. However, we have demonstrated that a temperature-independent phonon damping is experimentally observed for modes propagating along low-symmetry directions. It is only when the disorder, concerning 12 Al atoms, is appropriately introduced in the model that MD simulations do reproduce this observation. Using the Green-Kubo approach and MD simulations, the observed temperature dependence of the lattice thermal con-

ductivity is also reproduced by the disordered model only. Surprisingly, MD simulation with the ordered model leads to a weak  $T^{-0.50}$  decay of the thermal conductivity, much different from the  $T^{-1}$  obtained for three-phonon processes simulation. Our results pave the way to a detailed study of lattice dynamics and thermal transport properties of a broad range of materials with large unit cell, for which the interplay between long-range periodic order, structural complexity, local atomic clusters, and disorder is important.

## ACKNOWLEDGMENTS

This work has been carried out within the European C-MetAC network. We thank the ILL and the ESRF for the attribution of beam time. We thank A. Bosak for his help in setting up the IXS experiment at the ESRF. M.M. also acknowledges support from Slovak grant agency VEGA, Contract No. 2/0082/17.

## APPENDIX A

The response function  $S(\mathbf{Q}, \omega)$  associated with the absorption (emission) of one phonon in the state  $(s, \mathbf{q})$  writes

$$S_S(\mathbf{Q}, \omega)|_{\pm 1} \propto |F_{in,s}(\mathbf{Q}, \mathbf{q})|^2 \times \delta(\mathbf{Q} - \mathbf{Q}_{\text{Bragg}} + \mathbf{q}) \cdot \frac{n(\omega, T)|_{\pm 1}}{\omega} \delta[\omega - \omega_S(\mathbf{q})], \quad (\text{A1})$$

where

$$n(\omega)|_{\pm 1} = \exp\left(\frac{\hbar\omega}{k_B T} - 1\right)^{-1} + \frac{1}{2} \pm \frac{1}{2} \quad (\text{A2})$$

and  $|F_{in,s}(\mathbf{Q}, \mathbf{q})|^2$  is the inelastic structure factor. In the long-wavelength acoustic limit, this inelastic structure factor can be easily calculated, see expression (3).

## APPENDIX B

The comparison between the harmonic simulation using the ordered or disordered model is discussed in this Appendix. It is important to note that the computation of the response function  $S(\mathbf{Q}, \omega)$  is crucial when comparing with experiment since the dispersion relation of the disordered model contains an almost continuous distribution of modes. Indeed, the cell contains 1205 atoms and thus more than 3000 branches. This is illustrated in Fig. 15 which displays the dispersion relation for both models and both the high and low symmetry directions. When the mode density becomes too high to be distinguished as a single line, a color code is used from low mode density (gray) to high mode density (red). As can be seen, the dispersion relation rapidly becomes an almost continuous distribution of modes in the disordered model.

When computing the response function  $S(\mathbf{Q}, \omega)$  in a given point of reciprocal space, selection rules apply and only a limited number of modes are selected and visible. As explained in the main text, this is particularly important when the Lorentzian broadening is occurring for TA modes propagating along the low-symmetry directions. Indeed, this broadening could be due to the superposition of several modes (the mode density is already high at this energy in the disordered model) as was observed in the Zn-Mg-Sc icosahedral quasicrystal,

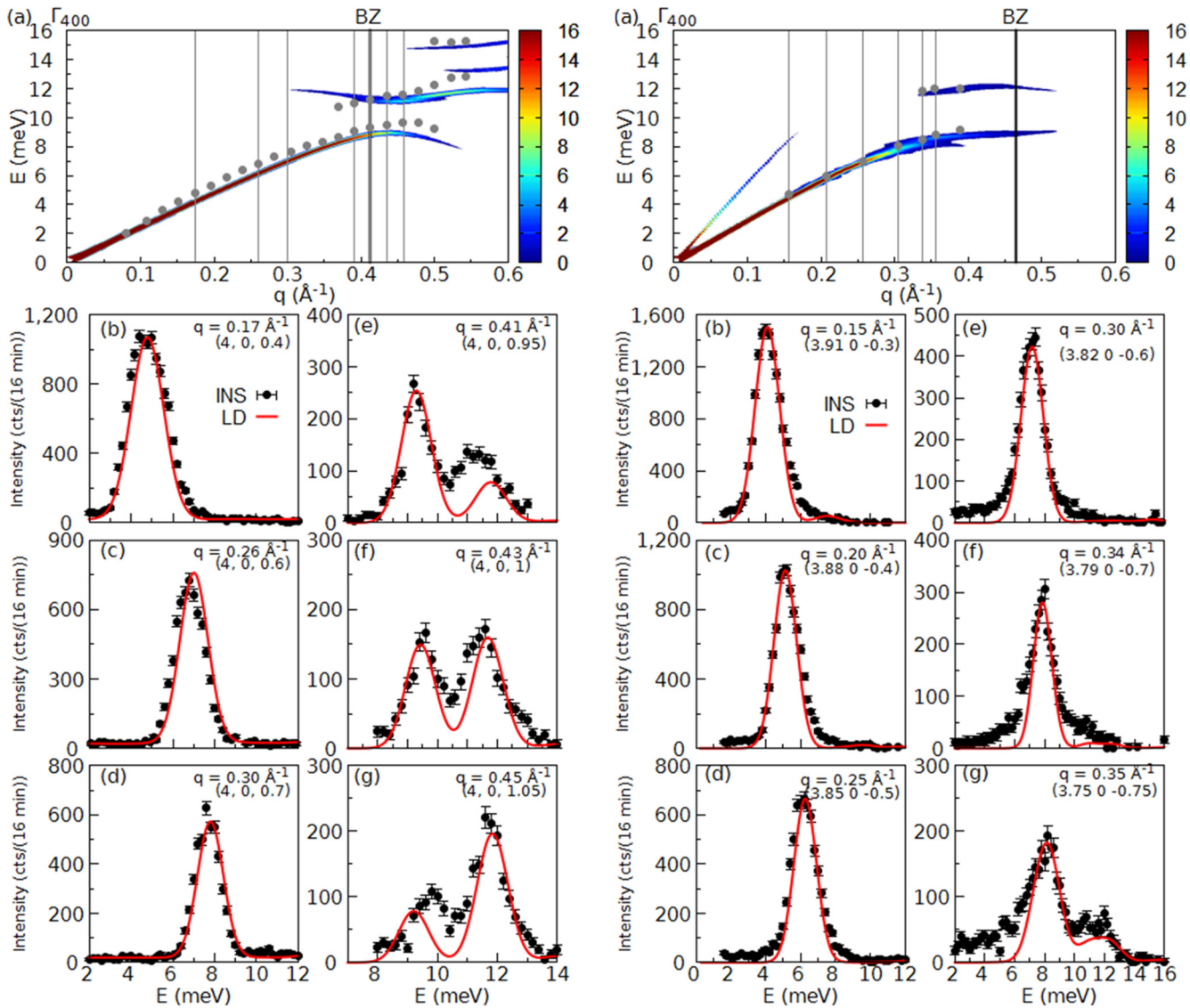


FIG. 17. Comparison between inelastic neutron scattering measurement and harmonic simulations using oscillating pair potentials and the disordered model for  $o\text{-Al}_{13}\text{Co}_4$ . The measurement has been carried out around the strong 400 Bragg peak and a single scale factor was used for all simulations. Left panel: TA modes propagating along the [001] high-symmetry direction and polarized along [100]. The quantitative agreement between experiment and simulation is excellent. Both the dispersion [shown in (a)] and the intensity distribution and gap opening [shown in (b)–(g)] are well reproduced. Right panel: TA modes propagating along the [103] direction. The dispersion relation [shown in (a)] and long-wavelength acoustic mode intensity [shown in (b)–(d)] are well reproduced. At higher energies the Lorentzian shape is not reproduced [(e)–(g)], although the intensity distribution is correctly reproduced.

for instance. This is not the case here, and it is illustrated in Fig. 10 where the harmonic simulation has been convoluted by a narrow Gaussian. Although the simulation with the disordered model is slightly broader than the one with the ordered model, only one major acoustic contribution is contributing in the simulation. A few much weaker opticlike excitations are also visible, but with a negligible intensity.

Using the ordered model instead of the disordered one does not change the low-lying acoustic branch. As expected from the above comparison, higher excitations have a broader distribution in the disordered model than in the ordered one. This is illustrated in Fig. 16 where the high-energy part of the spectrum is compared to both models: the simulation with the

disordered model has a significantly larger Bragg response function than the ordered one and compares better with experimental data.

## APPENDIX C

The full set of comparisons between neutron data and the harmonic simulation with the disordered model is given in this Appendix. Figure 17 gathers individual constant  $Q$  energy scans. Note that a single scale factor has been used for the simulation, leading to a very good agreement with experiment. In particular, the anticrossing, gap opening, and intensity transfer between the acoustic and optical branches

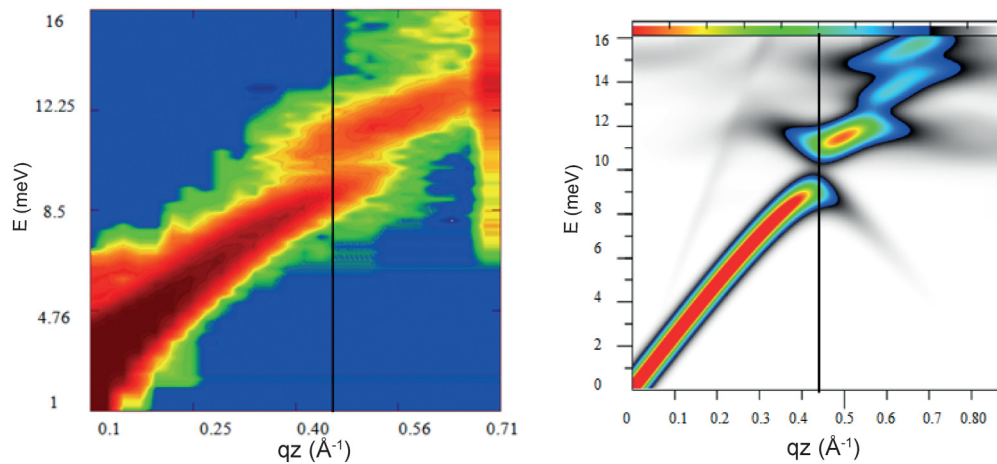


FIG. 18. 2D color representation of the inelastic scattering function for o-Al<sub>13</sub>Co<sub>4</sub> for TA modes propagating along the [001] direction. Left panel; experimental results obtained by inelastic neutron scattering; right panel simulation using the harmonic approximation and the ordered model.

are perfectly reproduced for modes propagating along the [001] direction. However, note the discrepancy for modes propagating in a low-symmetry direction [Figs. 17(e)–17(g)] for which the Lorentzian shape can not be properly reproduced.

Figure 18 displays results for the intensity distribution of the response function for TA modes propagating along the

[001] direction and polarized along [100], measured from the 400 zone center. The gap opening at the Brillouin zone boundary is clearly visible. It is compared to the simulation in the harmonic simulation with the ordered model. The agreement is excellent. In the acoustic region, a similarly good agreement is obtained with the disordered model (see above).

- [1] D. Shechtman, I. Blech, D. Gratias, and J. W. Cahn, *Phys. Rev. Lett.* **53**, 1951 (1984).
- [2] T. Janssen, G. Chapuis, and M. de Boissieu, *Aperiodic Crystals. From modulated phases to quasicrystals*, 2nd ed. (Oxford University Press, Oxford 2018).
- [3] M. de Boissieu, M. Boudard, R. Bellissent, M. Quilichini, B. Hennion, R. Currat, A. I. Goldman, and C. Janot, *J. Phys.: Condens. Matter* **5**, 4945 (1993).
- [4] K. Shibata, R. Currat, M. de-Boissieu, T. J. Sato, H. Takakura, and A. P. Tsai, *J. Phys.: Condens. Matter* **14**, 1847 (2002).
- [5] M. de Boissieu, R. Currat, S. Francoual, and E. Kats, *Phys. Rev. B* **69**, 054205 (2004).
- [6] M. de Boissieu, S. Francoual, M. Mihalkovic, K. Shibata, A. Q. R. Baron, Y. Sidis, T. Ishimasa, D. Wu, T. Lograsso, L. P. Regnault, F. Gahler, S. Tsutsui, B. Hennion, P. Bastie, T. J. Sato, H. Takakura, R. Currat, and A. P. Tsai, *Nat. Mater.* **6**, 977 (2007).
- [7] K. Urban and M. Feuerbacher, Structurally complex alloy phases, *J. Non-Cryst. Solids* **334**, 143 (2004).
- [8] M. A. Chernikov, A. Bianchi, and H. R. Ott, *Phys. Rev. B* **51**, 153 (1995).
- [9] J. Dolinšek, M. Komelj, P. Jeglič, S. Vrtnik, D. Stanič, P. Popčević, J. Ivkov, A. Smontara, Z. Jagličič, P. Gille, and Yu. Grin, *Phys. Rev. B* **79**, 184201 (2009).
- [10] M. Bobnar, P. Jeglič, M. Klanjšek, Z. Jagličič, M. Wencka, P. Popčević, J. Ivkov, D. Stanič, A. Smontara, P. Gille, and J. Dolinšek, *Phys. Rev. B* **85**, 024205 (2012).
- [11] G. S. Nolas, J. L. Cohn, G. A. Slack, and S. B. Schujman, *Applied Phys. Lett.* **73**, 178 (1998).
- [12] W. Steurer, *Z. Kristall. - Crystall. Materials* **219**, 391 (2004).
- [13] P. Gille and B. Bauer, *Cryst. Res. Technol.* **43**, 1161 (2008).
- [14] See Supplemental Material at <http://link.aps.org/supplemental/10.1103/PhysRevB.102.024303> for the following: (i) Figure 1 for a photograph of the large single crystal of the o-Al<sub>13</sub>Co<sub>4</sub> phase. (ii) Section S1 and Fig. 2 for a description of the columnar cluster observed in the o-Al<sub>13</sub>Co<sub>4</sub> phase. (iii) Section S1 and Fig. 3 for a list of coordinates of the re-refined structure of the o-Al<sub>13</sub>Co<sub>4</sub> phase. (iv) Section SIII for the constant  $Q$  energy scans data obtained by inelastic neutron (Figs. 6 and 7) and inelastic x-ray (Figs. 8 and 9) scattering carried out on the o-Al<sub>13</sub>Co<sub>4</sub> single crystal phase. The fitting by DHO is also shown. (v) Refer to Eigenvector-High-symmetry.gif (magdraw05\_mode\_2p1\_2p17meV.gif) for an animated picture of the eigenvectors of a transverse acoustic mode propagating along the [001] high-symmetry direction and polarized along [100] at the zone boundary, as calculated in the ordered o-Al<sub>13</sub>Co<sub>4</sub> phase. The stationary wave is clearly visible. (vi) Refer to Eigenvector-Low-symmetry.gif (magdraw10\_mode\_4p3\_2p797meV\_Amplitude\_1.gif) for an animated picture of the eigenvectors of a transverse acoustic mode propagating along the low-symmetry [103] direction at the zone boundary, as calculated in the ordered o-Al<sub>13</sub>Co<sub>4</sub> phase. The stationary wave is no longer visible. Weakly bounded Al atoms located inside the clusters present large vibrational amplitudes. (vii) Section II for details on the lattice thermal conductivity simulations using MD and the Green-Kubo method together with its validation on elemental germanium. See also Refs. [3–11] therein.

- [15] B. Hamelin and P. Bastie, *Proc. SPIE* **4786**, 29 (2002).
- [16] A. Guinier and J. Tenevin, *Acta Crystallogr.* **2**, 133 (1949).
- [17] J. Grin, U. Burkhardt, M. Ellner, and K. Peters, *J. Alloys Compd.* **206**, 243 (1994).
- [18] M. Mihalkovič and C. L. Henley, *Phys. Rev. B* **85**, 092102 (2012).
- [19] M. Armbrüster, R. Schlögl, and Yu. Grin, *Sci. Technol. Adv. Mater.* **15**, 034803 (2014).
- [20] P. Simon, I. Zelenina, R. Ramlau, W. Carrillo-Cabrera, U. Burkhardt, H. Borrmann, R. C. Gil, M. Feuerbacher, P. Gille, and Y. Grin, *J. Alloys Compd.* **820**, 153363 (2020).
- [21] F. Ercolessi and J. Adams, *Europhys. Lett.* **26**, 583 (1994).
- [22] V. Vitek, *MRS Bulletin* **21**, 20 (1996).
- [23] J. A. Moriarty and M. Widom, *Phys. Rev. B* **56**, 7905 (1997).
- [24] [www.ill.eu/fr/instruments-support/instruments-groups/instruments/in22/](http://www.ill.eu/fr/instruments-support/instruments-groups/instruments/in22/)
- [25] <http://neutron.ujf.cas.cz/restrax/>
- [26] <http://www.esrf.eu/home/UsersAndScience/Experiments/EMD/ID28/>
- [27] E. Burkel, *Rep. Prog. Phys.* **63**, 171 (2000).
- [28] M. Krisch and F. Sette, *Inelastic X-ray Scattering from Phonons: Light Scattering in Solid IX* (Springer, Berlin, 2007), pp. 317–370.
- [29] S. Pailh s, H. Euchner, V. M. Giordano, R. Debord, A. Assy, S. Gomes, A. Bosak, D. Machon, S. Paschen, and M. de Boissieu, *Phys. Rev. Lett.* **113**, 025506 (2014).
- [30] H. Schober, S. Petit, and S. Rols, *Les excitations dans la matiere condense. Vibrations et phonons.* (Editions de Physique, Paris, 2009).
- [31] <http://lammmps.sandia.gov/>.
- [32] <https://www.ill.eu/de/instruments-support/computing-for-science/cs-software/all-software/nmoldyn/>.
- [33] M. Kaviany, *Heat Transfer Physics* (Cambridge University Press, Cambridge, 2008).
- [34] H. Euchner, M. Mihalkovic, F. Gahler, M. R. Johnson, H. Schober, S. Rols, E. Suard, A. Bosak, S. Ohhashi, A. P. Tsai, S. Lidin, C. P. Gomez, J. Custers, S. Paschen, and M. de Boissieu, *Phys. Rev. B* **83**, 144202 (2011).
- [35] P. G. Klemens, *Phys. Rev.* **119**, 507 (1960).
- [36] P.-F. Lory, S. Pailh s, V. M. Giordano, H. Euchner, H. D. Nguyen, R. Ramlau, H. Borrmann, M. Schmidt, M. Baitinger, M. Ikeda, P. Tomeš, M. Mihalkovič, C. Allio, M. R. Johnson, H. Schober, Y. Sidis, F. Bourdarot, L. P. Regnault, J. Ollivier, S. Paschen *et al.*, *Nat. Commun.* **8**, 491 (2017).
- [37] T. Tadano, Y. Gohda, and S. Tsuneyuki, *J. Phys.: Condens. Matter* **126**, 225402 (2014).